Geophysical Journal International

Geophys. J. Int. (2010) **182,** 461–476 doi: 10.1111/j.1365-246X.2010.04632.x

Approximations in seismic interferometry and their effects on surface waves

W. P. Kimman and J. Trampert

Department of Earth Sciences, Utrecht University, PO Box 80021, *Utrecht* 3584 CD, *The Netherlands. E-mail: kimman@geo.uu.nl*

Accepted 2010 April 18. Received 2010 April 16; in original form 2009 October 14

SUMMARY

We investigate common approximations and assumptions in seismic interferometry. The interferometric equation, valid for the full elastic wavefield, gives the Green's function between two arbitrary points by cross-correlating signals recorded at each point. The relation is exact, even for complicated lossless media, provided the signals are generated on a closed surface surrounding the two points and are from both unidirectional point-forces and deformation-rate-tensor sources. A necessary approximation to the exact interferometric equation is the use of signals from point-force sources only. Even in simple layered media, the Green's function retrieval can then be imperfect, especially for waves other than fundamental mode surface waves. We show that this is due to cross terms between different modes that occur even if a full source boundary is present. When sources are located at the free surface only, a realistic scenario for ambient noise, the cross terms can overwhelm the higher mode surface waves. Sources then need to be very far away, or organized in a band rather than a surrounding surface to overcome this cross-term problem. If sources are correlated, convergence of higher modes is very hard to achieve. In our examples of simultaneously acting sources, the phase of the higher modes only converges correctly towards the true solution if sources are acting in the stationary phase regions. This offers an explanation for some recent body wave observations, where only interstation paths in-line with the prevailing source direction were considered. The phase error resulting from incomplete distributions around the stationary phase region generally leads to an error smaller than 1 per cent for realistic applications.

Key words: Interferometry; Surface waves and free oscillations; Wave propagation.

GJI Seismology

1 INTRODUCTION

Seismic interferometry is a relatively young and fast expanding field both theoretically and experimentally (see reviews by Campillo 2006; Curtis *et al.* 2006; Gouédard *et al.* 2008a; Snieder *et al.* 2009). It allows to reconstruct the Green's function between two receivers by cross correlating the signals received at both receivers. A first mathematical demonstration of the principle was provided by Lobkis & Weaver (2001) assuming that the wavefields were diffuse. A more general demonstration based on representation theorems was given by Wapenaar (2004). Experimental proof was given by Weaver & Lobkis (2001), Campillo & Paul (2003), Larose *et al.* (2004) and Malcolm *et al.* (2004). An elegant intuitive derivation of the principle is given by Derode *et al.* (2003), who showed the connection between interferometry and time reversal, and Snieder (2004) who applied stationary phase principles. Since then a vast number of applications have been proposed (Campillo 2006; Curtis *et al.* 2006; Gouédard *et al.* 2008a; Snieder *et al.* 2009). Most applications have been in ambient noise tomography (e.g. Sabra *et al.* 2005; Shapiro *et al.* 2005; Yang *et al.* 2007; Picozzi *et al.* 2009; Nishida *et al.* 2009). In these studies, only the fundamental mode surface wave is retrieved. Our main motivation is to focus on the retrieval of overtones. Overtones are of great interest for imaging because they could substantially reduce uncertainties in tomography and improve depth resolution. Although body wave observations have been reported in noise studies (Roux *et al.* 2005b; Gerstoft *et al.* 2008), often only the fundamental mode surface waves are retrieved. The identification of reflections (Draganov *et al.* 2007, 2009) require a great deal of processing to remove the surface wave component. In this study we investigate the possibility to retrieve higher modes in detail.

The most general demonstration of the interferometric theorem is based on representation theorems of the correlation type (de Hoop 1995). Wapenaar (2004) and van Manen *et al.* (2006) showed that the Green's function between two arbitrary points is given by

$$G_{im}(\mathbf{x_A}, \mathbf{x_B}, \omega) - G^*_{im}(\mathbf{x_A}, \mathbf{x_B}, \omega) = -\oint_S \big[G_{in}(\mathbf{x_A}, \mathbf{x}, \omega) n_j c_{njkl} \partial_k G^*_{ml}(\mathbf{x_B}, \mathbf{x}, \omega) - n_j c_{njkl} \partial_k G_{il}(\mathbf{x_A}, \mathbf{x}, \omega) G^*_{mn}(\mathbf{x_B}, \mathbf{x}, \omega)\big] \mathrm{d}S \quad (1)$$

The left-hand side represents the particle displacement (in the frequency domain) in the i-direction at location $\mathbf{x_A}$, due to an impulsive point force in the m-direction at $\mathbf{x_B}$. The asterisk denotes complex conjugation. The source positions $\mathbf{x}$ are located on an arbitrary enclosed surface S with normal n_j. The term $n_j c_{njkl} \partial_k G_{il}(\mathbf{x_A}, \mathbf{x}, \omega)$ represents the particle displacement at $\mathbf{x_A}$ due to a deformation-rate-tensor source at $\mathbf{x}$. Here ∂_k is the partial derivative in the k-direction of the Green's function, and c_{njkl} the stiffness tensor at the source location. Eq. (1) is exact for a full wavefield in any lossless elastic medium. The theory can be extended to attenuating media if interferometry by deconvolution (Wapenaar *et al.* 2008) is applied. The Green's function between points $\mathbf{x_A}$ and $\mathbf{x_B}$ can thus be reconstructed from a summation of cross correlations between a Green's function at one receiver, and the traction associated to a Green's function at the other. Invoking reciprocity (Aldridge & Symons 2001) one could consider recording the gradient of the wavefield (Curtis & Robertsson 2002) to replace the tractions associated to the Green's function. This would however require more complicated recording configurations (involving buried receivers) than usually available, and the knowledge of the local stiffness parameters. Instead, an approximation is made to replace the traction (often referred to as a dipole source) by a scaled Green's function or displacement (often referred to as a monopole source). If the wavefield is diffuse and the energy is equipartitioned (i.e. all elastic modes are excited with the same amplitude), the approximation leads to the correct Green's function (Weaver & Lobkis 2001).

In the real Earth, the distribution of noise sources is not uniform. This can be a further problem for retrieving the Green's function. At around 1 Hz, seismic noise is generated from wind and local meteorological conditions, while higher frequency noise (>1 Hz) originates mostly from human activities (Bonnefoy-Claudet *et al.* 2006a). Lower frequency (<0.5 Hz) noise sources have an oceanic origin. Microseisms are thought to originate from surface pressure oscillations caused by the interaction between opposite travelling waves that have the same frequency in the ocean wave spectrum (Longuet-Higgins 1950). The exact mechanism of coupling however is unknown. Microseismic sources can be very limited in aperture and seasonally dependent (Stehly *et al.* 2006; Tanimoto *et al.* 2006). Furthermore, local storms and hurricanes can prove to be microseismic sources (Gerstoft *et al.* 2008). In general, noise sources are thought to act close to the surface (Rhie & Romanowicz 2004). In the following, we investigate the effect of imperfect source distributions in azimuth, and configurations with free surface sources only, on the success of the Green's function retrieval.

For non-diffusive waves, an expression for isolated surface wave modes in the far field has been derived with the stationary phase approximation (Halliday & Curtis 2008).

$$G_{im}(\mathbf{x_A}, \mathbf{x_B}, \omega) - G^*_{im}(\mathbf{x_A}, \mathbf{x_B}, \omega)$$
$$\approx -2i\omega \oint_S A(\omega) G_{ip}(\mathbf{x_A}, \mathbf{x}, \omega) G^*_{mp}(\mathbf{x_B}, \mathbf{x}, \omega) \mathrm{d}S, \qquad (2)$$

where $A(\omega)$ is a frequency-dependent scale factor. The repeated subscript p indicates a summation of x-, y-, and z-directional point forces at every source location on the surrounding integration surface. The term $i\omega$ in the frequency domain is equivalent to taking a time derivative in the time domain. Eq. (2) is always valid for isolated surface wave modes. The expression can be summed on both sides over all modes to yield the full Green's function. Halliday & Curtis (2008) predict that the cross terms cancel in the far field approximation. This summation requires that pure mode Green's functions are recorded (right-hand side of eq. 2), but in real applications the wavefield is multimode, and the frequency-dependent amplitude factor $A(\omega)$ is unknown and ignored. The notation of Wapenaar & Fokkema (2006) considers the complete wavefield and gives a similar result, but sources are expressed in pure P- and S- wave potentials. We generated seismograms using a 3-D finite-difference code (Kristek *et al.* 2002; Moczo *et al.* 2002) which calculates displacements and stresses. The computed wavefields are from uncorrelated sources (sequentially fired) on a surrounding surface. We first applied eqs (1) and (2) in a homogeneous medium. This is the canonical case described in Sanchez-Sesma & Campillo (2006), where the necessary conditions for equipartitioning are satisfied in the far field. We find that the recovered Green's function matches the directly computed Green's function for both equations (Fig. 1). The result is perfectly antisymmetric around t = 0, but for clarity we only plot the causal part. However, as soon as

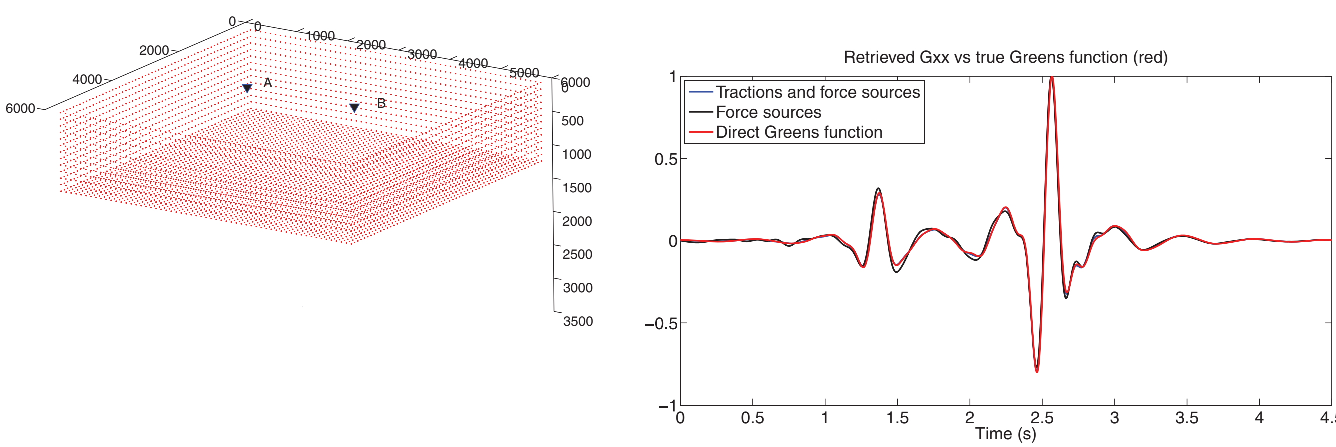

Figure 1. On the left-hand side, the typical rectangular source distribution (red dots) used for Figs 1 and 2. This configuration is chosen since it is the simplest shape to compute the normals in eq. (1), which puts no constraints on the integration shape. The normals at the edge points are taken $(\pm\frac{1}{2}\sqrt{2}, \pm\frac{1}{2}\sqrt{2}, 0)$. Dimensions for this example, that of a homogeneous half-space, are 2730 × 1330 m, with a spacing of 7 m. No sources on top of the free surface are required (Wapenaar 2004). The retrieved component G_{xx} is compared to the directly computed response (red). The two receivers are located at the free surface, in-line in the x-direction with an interstation distance of 2100 m. The Green's function, composed of a direct P, and a Rayleigh wave is retrieved with minor differences. Medium properties are: $V_p = 1200\,\mathrm{m\,s^{-1}}$, $V_s = 700\,\mathrm{m\,s^{-1}}$ and $\rho = 1100\,\mathrm{kg\,m^{-3}}$. The resulting Rayleigh wave phase velocity is $642.7\mathrm{m\,s^{-1}}$. Plotted is the causal part of the retrieved Green's function correlated with the source wavelet. All sources are uncorrelated and have the same spectrum, near flat between 2–8 Hz. For computational simplicity, the sources and receivers are interchanged using reciprocity. Since a staggered FD grid is used there is also a slight discrepancy between the different positions for displacements and stresses.

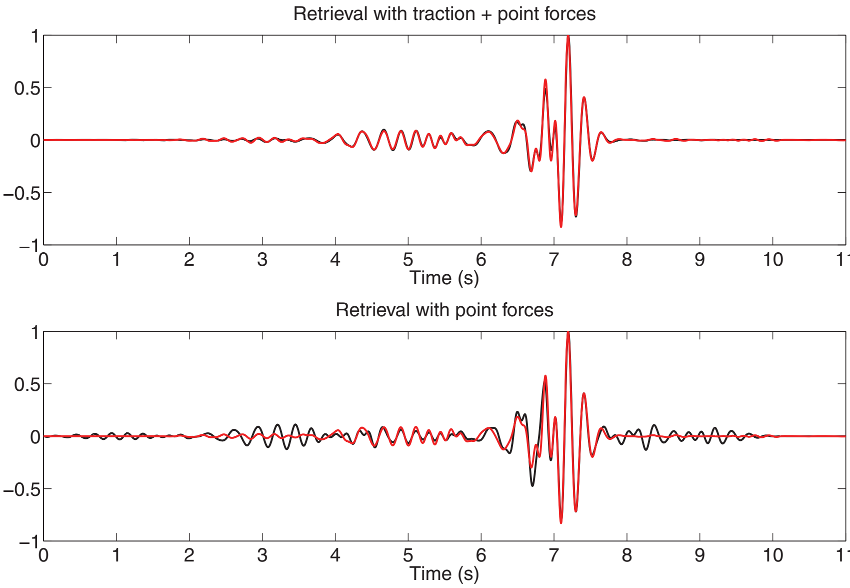

Figure 2. Retrieval (black) for the layered model in Table 1, using eq. (1) (top panel), versus the result using three orthogonal point forces only (bottom panel). The interstation distance is 2940 m in this example. Dimensions of the source grid are 5691 x 1606 m, with a spacing of 7 m. Almost all frequencies satisfy the far field approximation, and the very dense sampling excludes aliasing effects. The approximate equation fails where the exact equation perfectly retrieves the true Green's function (red). From the model in Table 1, we know that the Green's function contains three overtones arriving at the same time before the fundamental mode.

the medium is complicated by introducing layering, the monopole approximation shows amplitude differences and spurious arrivals (Fig. 2). The amplitude differences are to be expected since we neglected the unknown scaling $A(\omega)$, but the spurious arrivals are surprising. Snieder *et al.* (2006) first identified spurious arrivals in the case of inhomogeneous source distributions. Halliday & Curtis (2008) also identified spurious events for imperfect source distributions, and showed that they are due to cross terms between different modes. In our experiments, we find that the spurious arrivals exist even with a perfect source distribution (of a surrounding surface), and we will show that these are due to these same cross terms. This could be important for the retrieval of overtones because they might arrive at the same time. Throughout the remainder of the paper we consider retrieval in a half-space between two stations located at the free surface. In this case, the complete wavefield can be described by a superposition of modes (Nolet *et al.* 1989; Snieder 2002). Since surface waves dominate the Green's function retrieval, it is most convenient to express displacements as a sum of surface wave modes. Halliday & Curtis (2008) showed that expression (2) is correct for an isolated mode in the far field. We will adopt this mode representation and in the following investigate displacements calculated using surface wave mode summation (Herrmann 1978).

2 GREEN'S FUNCTION RETRIEVAL USING MONOPOLE SOURCES WITH A PERFECT DISTRIBUTION

2.1 Single mode Rayleigh waves

Eq. (2) follows from substituting the Rayleigh wave Green's function (Aki & Richards 2002) into the exact interferometry equation. The spatial derivative of the Green's function can be expressed by a term proportional to the Green's function itself. We assume a cylindrical distribution of sources (Fig. A1) and the layered medium described in Table 1. The Green's function can then be represented as

Table 1. A 1-D layered elastic medium with no attenuation.

	Thickness (m)	Vp (m s^{-1})	Vs (m s^{-1})	Density (kg m^{-3})
Layer 1	45	850	500	1350
Layer 2	45	1050	650	1450
Layer 3	90	1400	850	1450
Half-space	–	1850	1050	1950

$$G_{im}(\mathbf{x_A}, \mathbf{x_B}, \omega) - G^*_{im}(\mathbf{x_A}, \mathbf{x_B}, \omega) \approx -2i\omega U(\omega) \int_0^\infty \int_0^{2\pi} \rho G_{ip}(\mathbf{x_A}, \mathbf{x}, \omega) G^*_{mp}(\mathbf{x_B}, \mathbf{x}, \omega) r \, d\phi dz, \quad (3)$$

(Appendix A and Halliday & Curtis 2008). The frequency-dependent scaling in eq. (2) is given by $A(\omega) = 2U(\omega)\rho$, where U is the group velocity of the specific surface wave mode, and ρ the density at the location of the source (r is the radius of the source cylinder). The approximation made in the derivation of eq. (3) is that the source-receiver distance is far compared to the interstation distance. This requirement is met by fixing the interstation distance to 15 km, and the source radius to 100 km, and choosing the passband filter between 0.5 and 9 Hz. 1800 regularly spaced sources per depth slice were used and integration performed to the depth where the eigenfunctions become negligible. Displacement seismograms resulting from point forces are computed by mode summation (Herrmann 1978). We confirm that the retrieved and the directly computed fundamental mode Green's function are identical (Fig. 3). We also confirm the derivation of Halliday & Curtis (2008) that the Green's function of the complete wavefield can be found by repeating this process for all individual modes in the corresponding wavefield. If for each source the individual mode response and the corresponding group velocity are known, the individually retrieved modal Green's functions can be summed. The result of this operation matches the full displacement waveform directly calculated using a point force (Fig. 3, bottom panel).

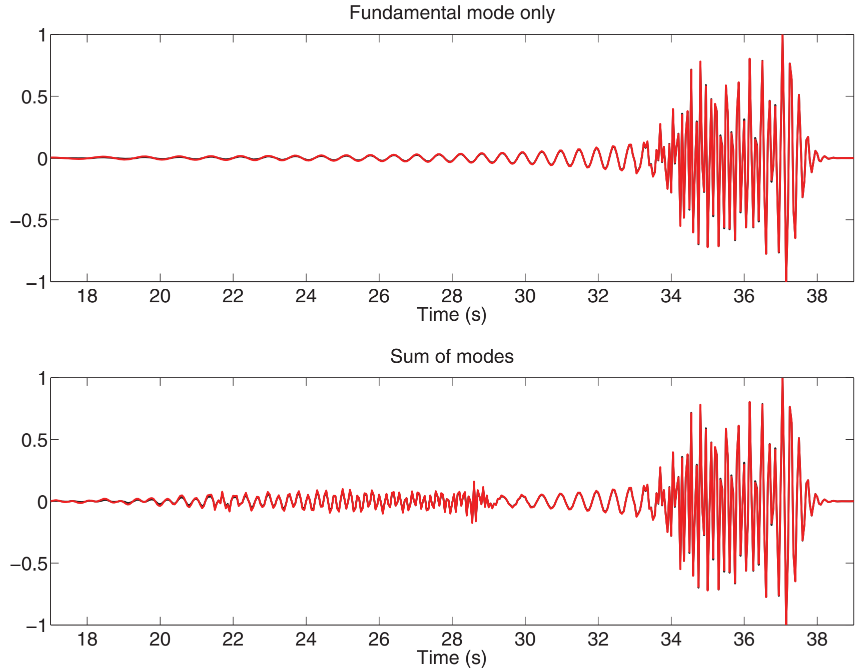

Figure 3. The top panel shows retrieval of the fundamental mode, according to eq. (3), in red. It correctly matches the directly computed Green's function (red). The sum of the retrieved Green's function for individual modes is shown on the bottom panel. Again this matches the directly computed Green's function of the complete wavefield (red).

2.2 Intermodal cross terms

For real data applications, eq. (3) forms the basis of seismic interferometry. By correlating total displacement rather than individual modes one assumes that any interaction between different modes can be ignored. Also, no $A(\omega)$ will be appropriate for a displacement composed from several modes and amplitude errors should be expected. In practice, with real (noise) data, this scaling is ignored, with the understanding that amplitude information is incorrect anyway because of an uneven excitation of noise sources, pre-whitening of the data, 1-bit correlation, etc. Next to the expected amplitude errors, we also noticed phase errors and spurious arrivals in the retrieved Green's function using the approximate equation (Fig. 2). Neglecting the frequency dependent scaling, we can make the summation of the retrieved Green's functions from isolated modes.

$$\sum_n \left[G^n_{im}(\mathbf{x_A}, \mathbf{x_B}, \omega) - G^{*n}_{im}(\mathbf{x_A}, \mathbf{x_B}, \omega)\right]$$
$$\approx -2i\omega \int_0^\infty \int_0^{2\pi} \left(\sum_n G^n_{ip}(\mathbf{x_A}, \mathbf{x}, \omega) G^{*n}_{mp}(\mathbf{x_B}, \mathbf{x}, \omega) + \sum_n \sum_{n' \neq n} G^n_{ip}(\mathbf{x_A}, \mathbf{x}, \omega) G^{*n'}_{mp}(\mathbf{x_B}, \mathbf{x}, \omega) \right) r\,\mathrm{d}\phi\,\mathrm{d}z. \tag{4}$$

The cross terms are defined by the cross correlation between modes of different mode identification number ($n \neq n'$). The total wavefield (left-hand side of equation 4) is obtained by the sum of cross correlations of the individual modes. We showed this above (Fig. 3). Hence the cross terms in the right-hand side of eq. (4) should sum to zero if we were to retrieve the correct Green's function. Snieder (2004) and Halliday & Curtis (2008) conclude that cross terms can be ignored under certain assumptions.

In Fig. 4 we show retrieval obtained by eq. (3) applied on a full wavefield, without scaling factor but with a perfect surrounding source surface. The reference Green's function is calculated from the sum of separately retrieved modes, also computed without taking into account $A(\omega)$ (therefore only different from the true Green's function by a small mode-dependent amplitude factor). Some noisy arrivals can be distinguished, implying that the cross terms have not completely cancelled. To verify this, we show the difference between the full wavefield correlation and reference Green's function in the lower panel. It corresponds exactly to the cross-term interactions, computed (also without scaling factor) one by one and summed. This demonstrates that eq. (3) leads to phase and amplitude errors even if the source distribution is perfect.

It seems puzzling to explain this in the light of the analysis of Halliday & Curtis (2008). Based on an orthogonality argument (their equation 9), the cross terms cancel. This is correct, but it should be noted that this relation holds for cross terms of polarization and traction vectors, and hence are for the exact interferometric eq. (1). The result in Fig. 2 shows that the cross terms indeed cancel when eq. (1) is used. Fig. 4 shows that when a full wavefield is inserted in eq. (2) or (3), cross terms do not cancel, an illustration of the fact that the orthogonality relation in terms of polarization only (Halliday & Curtis 2008, equation D-7) is not exact. Halliday & Curtis (2008) further showed an example where integration is performed fully around the two stations, where no stationary phase points exist for the cross-mode correlations. In our example, however, it appears that a complete integration surface alone is not enough for the exact cancellation of these terms. As we will show below, the distance to the sources crucial.

2.3 Love waves

Unless we have a special source-receiver geometry, the full wavefield contains Love waves as well as Rayleigh waves. The approximate interferometric equation for single-mode Love waves can be derived in a similar way to that for Rayleigh waves. It is less involved since the expression for the Love wave Green's function is

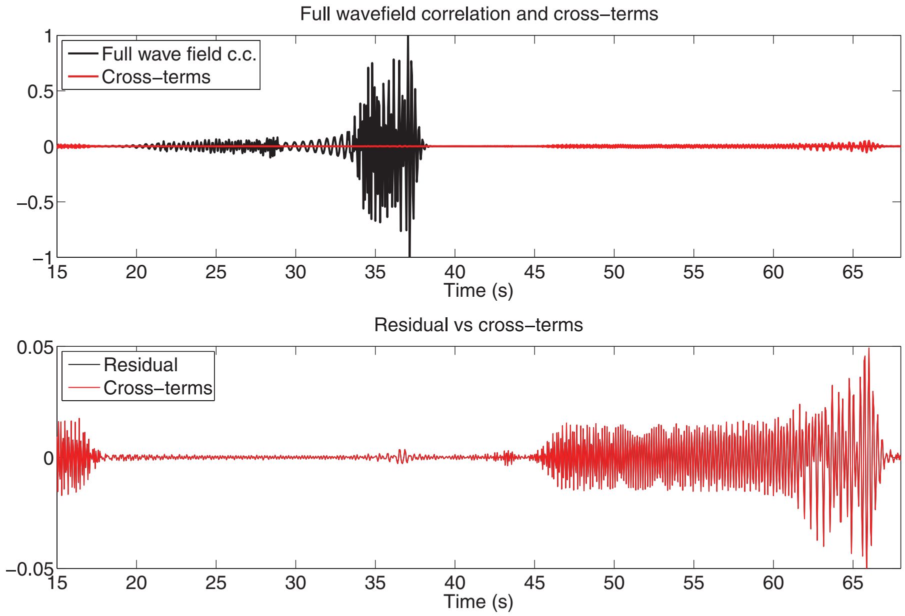

Figure 4. The Green's function obtained by applying eq. (3) [ignoring $U(\omega)$] to the full wavefield is shown (black), together with the explicitly computed cross terms (red). On the bottom we show the difference between the exact and retrieved Green's function (black). It exactly matches the cross terms (red).

simpler (Aki & Richards 2002). In Appendix B, we show that we obtain again eq. (3), but now $U(\omega)$ is the Love wave group velocity of the specific mode under consideration. There is a complete similarity between Love and Rayleigh waves, therefore we do not show examples of pure Love wavefields. Instead, we investigate the possible interaction between Love and Rayleigh waves, which could be another source for cross terms.

2.3.1 Love–Rayleigh interaction in the cross correlation

We use the same cylindrical source configuration as before to retrieve the G_{xx} component of the Green's tensor, now using a wavefield containing Love and Rayleigh wave fundamental modes. Since the stations are oriented in the x-direction, the total Love wave contribution should be zero. The obtained cross correlation indeed is exactly the same as the pure Rayleigh wave Green's function. Cross terms resulting from Love–Rayleigh mode interaction appear in the individual traces. The summation over this isotropic source distribution however leads to their cancellation.

Next, we consider the case of strong source directionality, or an inhomogeneous source distribution. In Fig. 5 we show the contributions from all sources as a function of angle ϕ in the integration surface. The source strength as a function of azimuth is shown (top panel), together with the correlation gathers (positive time only). The main source contribution arrives off the interstation path, located at $\phi = 0^\circ$, and a small variability is introduced. The second panel shows the case where Love and Rayleigh waves are used, the third panel the case where Love waves are excluded and the bottom panel their difference. This difference gather corresponds to pure Love wave information, and (the much smaller) Love–Rayleigh cross terms. With complete and homogeneous source coverage, such a gather sums to zero for G_{xx} (Fig. 6), because of the lack of stationary points. With the inhomogeneous source distribution, however, Love energy does not cancel and appears in the G_{xx} component of the retrieved Green's function, as illustrated in Fig. 6. Since Love waves in general travel faster, these false arrivals will always appear before the fundamental mode Rayleigh wave. Encouraging is the stability of the retrieved fundamental mode Rayleigh wave.

3 GREEN's FUNCTION RETRIEVAL USING MONOPOLE SOURCES AT THE SURFACE ONLY

3.1 Single mode Rayleigh waves

Microseisms are thought to originate near coastal areas and close to the Earth's surface. With sources at the free surface only, the requirement of an enclosing integration surface is not met. To study the effect of this source distribution, we repeat our previous analyses, but include sources at the free surface only. Therefore they are circularly distributed around the two receivers. Although the integration surface is incomplete, surface waves travel with the same phase velocity independent of the depth of excitation (Aki & Richards 2002). Any error introduced is therefore in amplitude only. This was already noted by Halliday & Curtis (2008). The relative amplitude errors however can be significant. We show one example in Fig. 7, for a first Rayleigh wave overtone retrieved using eq. (3). The correct scaling is applied but only horizontal forces are present at the free surface. It is one of the more extreme examples of a perfectly retrieved phase, but where the amplitude error could bias the group velocity measurement (e.g. with frequency-time analysis) of this mode.

3.2 Cross terms overwhelm higher modes

To investigate the importance of the uncancelled cross terms discussed earlier, we consider full wavefield correlations with sources at the free surface source only. Halliday & Curtis (2008) show, that spurious events due to cross terms can then occur, depending on the source distribution at the surface. Retrieval of the Green's function is considerably worse (Fig. 8) compared to the case of perfect source coverage. First, now the amplitude of higher modes

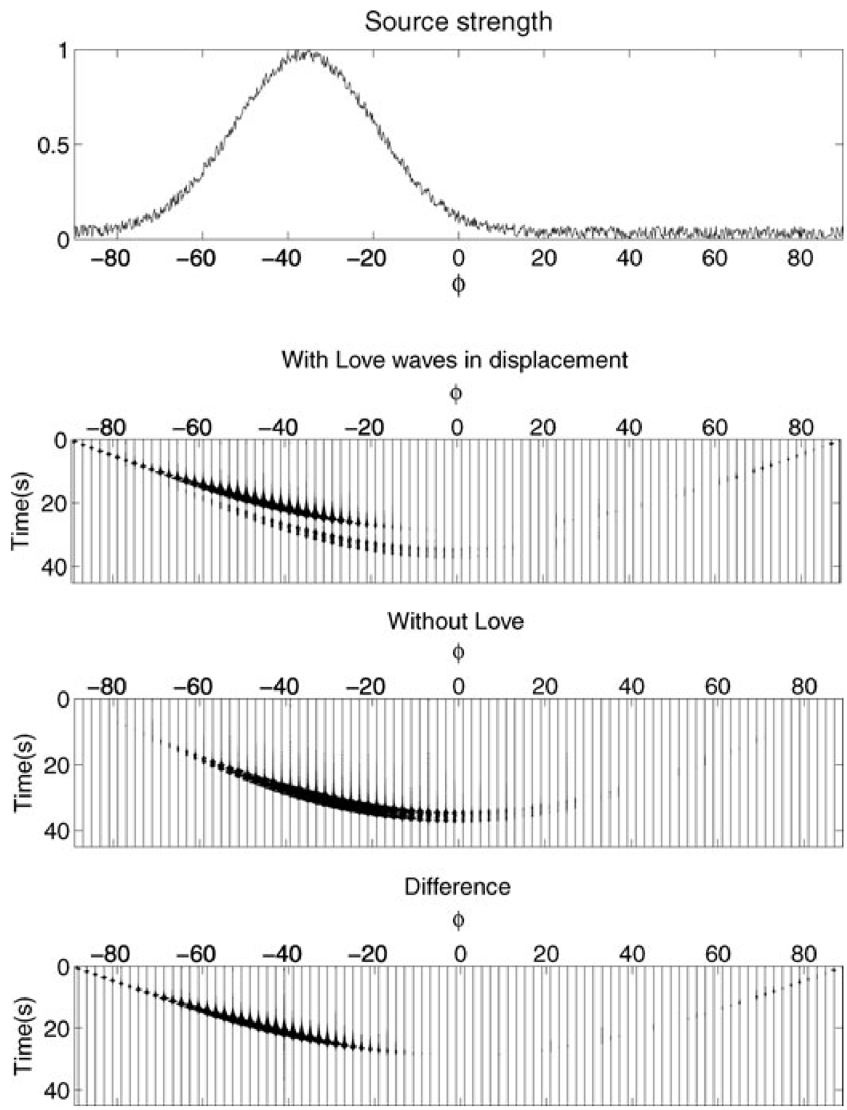

Figure 5. The cross correlation gathers showing the contribution in every source direction with a strong source directionality (top panel). The contributions from all depths have been summed. In the second panel, displacements are composed of both Love and Rayleigh wave fundamental modes, in the third panel only the Rayleigh wave fundamental mode is used. In the bottom panel their difference is shown. Only the causal part is plotted. For clarity only every 10th source position is shown.

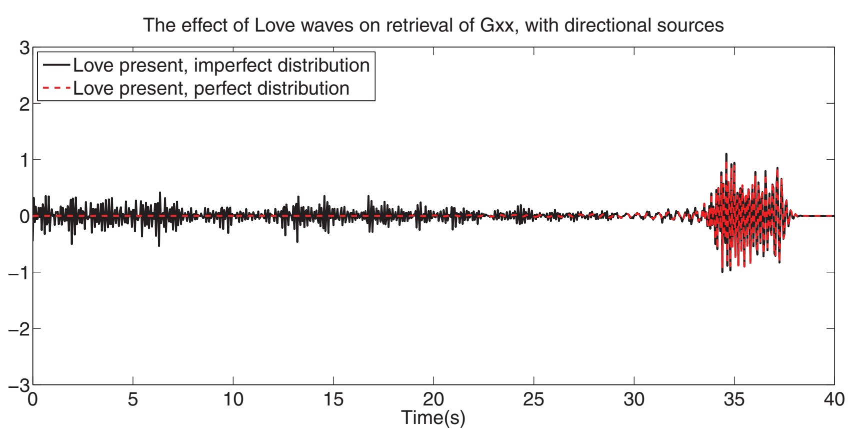

Figure 6. Illustration of spurious Love wave energy in the G_{xx} component of the Green's tensor. The spurious arrivals are caused by incomplete cancellation of Love wave energy (and Love–Rayleigh cross terms to a smaller extent.) With a complete source distribution, the Love contribution and Love–Rayleigh cross terms cancel (red-dashed).

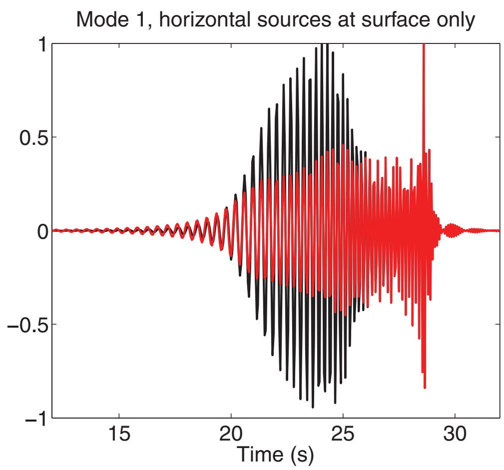

Figure 7. Retrieved first overtone, resulting from horizontal sources at the free surface. The retrieved Green's function (black) shows a mismatch, which is in amplitude only. The difference is a frequency-dependent amplitude factor, which can be significant though.

in the seismograms is smaller relative to the fundamental mode. This is because the fundamental mode is generally better excited by surface sources than overtones. Missing sources at depth therefore lead to smaller relative amplitudes for overtones. Neglecting the scaling factor makes higher modes even weaker because their group velocity is higher than that of the fundamental mode. Second, with the incomplete source distribution the amplitude of the cross terms become larger (Fig. 8). The consequence is that they become large enough to completely mask the higher modes and the retrieved Green's function contains cross terms of a magnitude comparable to that of the higher modes. We confirm that as in Halliday & Curtis (2008) with a homogeneous distribution over the free surface, or a thick boundary region of sources (e.g. Fig. 13), the cross terms diminish. Also Draganov *et al.* (2004) find that an irregularly (thick) boundary region reduces the effect of ghost terms associated with heterogeneities.

The question remains, whether or not cross terms will vanish if the assumption of a source boundary very far away is satisfied, for both the case of the enclosing integration surface and the case of sources at the surface only. We have seen, that cross terms are zero when both point-forces and deformation-rate tensor sources are used, but not when point forces alone are used. This means, that the expression regarding source excitation (implicit in the approximate equation) over the integration surface

$$\int \rho \left(r_1^n r_1^{n'} - r_2^n r_2^{n'} \right) \mathrm{d}S, \tag{5}$$

(n and n' representing different modes, r_1 and r_2 are the horizontal and vertical Rayleigh eigenfunctions) is in general not zero, neither for an enclosing surface nor with sources at the surface. We now increase the source radius with respect to the receiver interstation distance, in the case of sources at the surface (Fig. 9). The total energy of the cross terms over the time-series remains constant (bottom-right). However, the cross-term signal shifts away from zero and outside the time window of interest, as a result of the differences in group velocity of the different modes. Thus, cross terms remain even if the source boundary could be placed at infinity. However, they pose no problem to the time window of interest.

4 GREEN'S FUNCTION RETRIEVAL USING SOURCES WITH AZIMUTHAL HETEROGENEITY

4.1 Phase errors for a non-dispersive Rayleigh wave

Examples of the distribution of noise sources determined by back-projection or beamforming from real data can be found in Stehly *et al.* (2006) and Yao *et al.* (2009). They clearly indicate very limited source distributions. Gouédard *et al.* (2008b) demonstrated the ability to retrieve Green's function dispersion curves with directional noise. However, the success of interferometry depends on the presence of sources in the zone of constructive interference, or stationary phase region (Snieder 2004; Larose 2005; Roux *et al.* 2005a). If sources are absent in this region, the Green's function

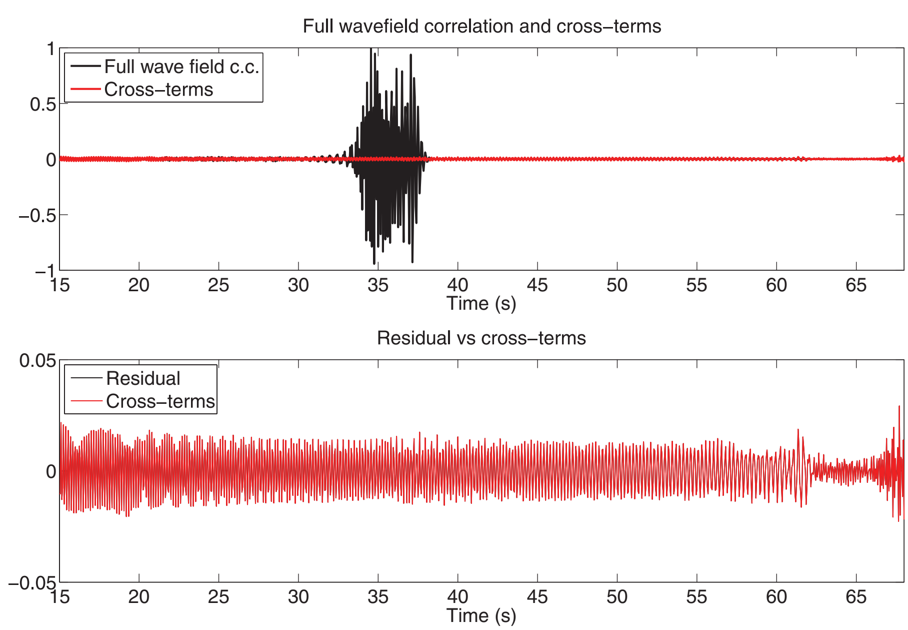

Figure 8. Same as Fig. (4) but for sources at the free surface only.

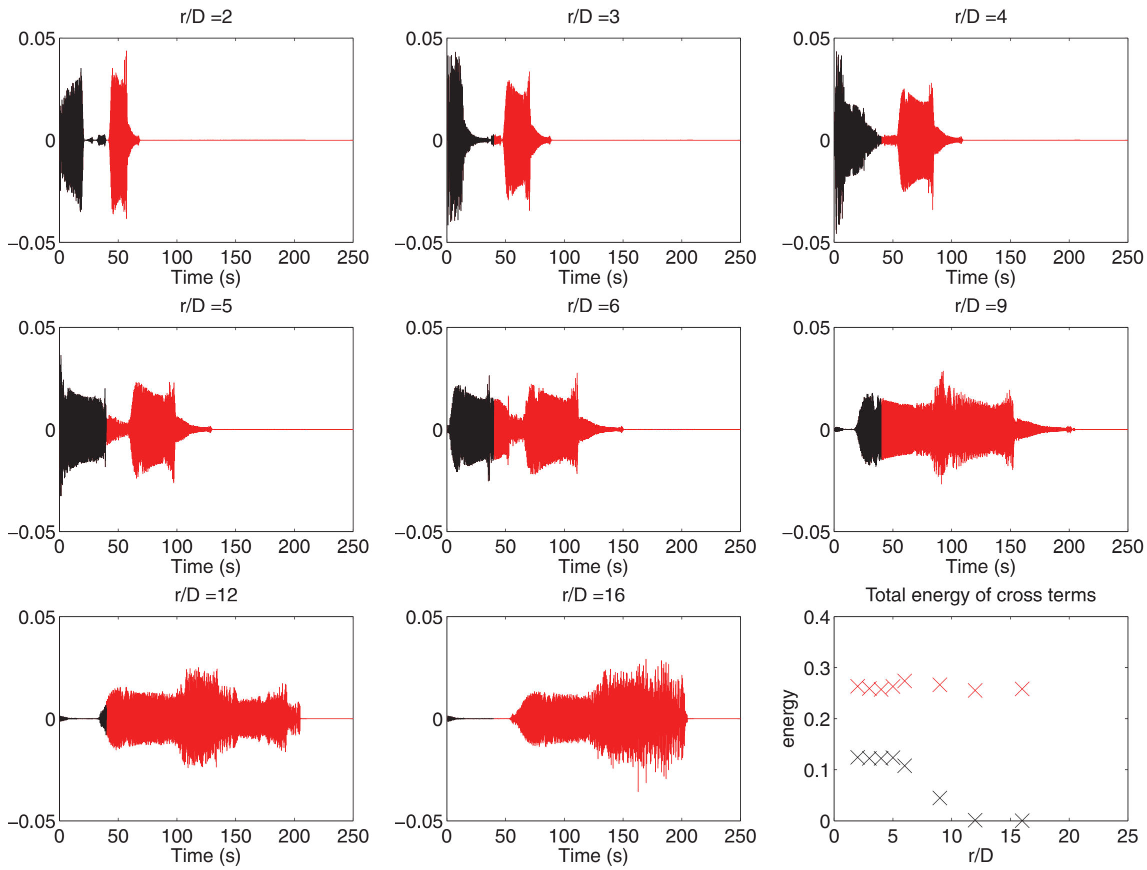

Figure 9. Cross terms as we increase the source radius. We plot the first 40 s in black (time window of interest). The amplitude is relative to the maximum amplitude of the Rayleigh wave. The total energy in the selected window (black), and in the total time-series (red) is shown (bottom-right panel). While the cross terms never disappear, due to the differences in group velocity between different modes they shift away from the time window of interest. In this example, this means when the source radius $r > 12$ times the interstation distance D.

retrieval will fail. Furthermore, if sources have a pre-dominant azimuthal distribution, the retrieved Green's function can be biased (Snieder *et al.* 2006; Mehta *et al.* 2008). Efforts have been made to only extract the Green's function with sources near the great circle of both receivers (Roux *et al.* 2005b), or to correct for the introduced bias (Roux 2009; Yao & van der Hilst 2009).

When sources are only located on the great circle of both receivers (and not over the entire stationary phase region), the Love and Rayleigh Green's functions have a phase shift of $\pi/4$ (Aki & Richards 2002) compared to the cross correlation which measures a time-shift only (Bensen *et al.* 2007; Tsai 2009). Therefore, an incomplete source distribution can cause phase shifts compared to the exact Green's function anywhere between 0 and $\pi/4$. We place sources on a circle around two receivers and vary their distribution by gradually increasing the number of sources from the interstation line. We measure the phase difference of the fundamental mode Rayleigh wave as a function of angular distribution (Fig. 10). We start at $\phi = 0$ (only one source), and gradually increase the coverage to $\phi = \pm 90^\circ$ (complete coverage for a one-sided Green's function) and measure the phase difference with respect to the true Green's function. The phase difference is measured by $\mathrm{d}\phi = \bar{\omega}\mathrm{d}t$, where $\bar{\omega}$ is the average angular frequency, and $\mathrm{d}t$ the time difference as measured by cross correlation. Coverage remains symmetric around the stationary phase point, an ideal situation, but very instructive. Snieder (2004) has shown that only sources at the stationary points contribute to the integral in eq. (2). These stationary points arise because of constructive interference and lie within a hyperbola which is defined by the wavelength λ, the interstation distance D and the assumed maximum phase difference for interference. Larose (2005) gives an expression for this angle as

$$\Phi \approx \pm\sqrt{\frac{\lambda}{3D}}, \tag{6}$$

assuming that waves interfere if their phase differs by less than $\pi/3$. We show three examples of different interstation distances (Fig. 10). These examples are for a homogeneous medium to visualize the behaviour of a non-dispersive Rayleigh wave for a relatively small frequency bandwidth. The phase-error decreases fast with increasing angle confirming Snieder's (2004) stationary phase arguments. It is interesting to note that expression (6) underestimates the angle of necessary coverage by a factor of 2.

4.2 Phase errors for a dispersive wave

To investigate this phase problem for dispersive waves, we consider again a layered medium (Table 2) and repeat the procedure described. We consider frequencies between 0.1 and 1.0 Hz, take the interstation distance to be 40 km and place sources at 2000 km distance. For each frequency, we measure the phase shift from the exact Green's function. The wavelength depends on frequency. The source coverage can therefore be sufficient for part of the frequency band, while other frequencies show too large phase errors. It is

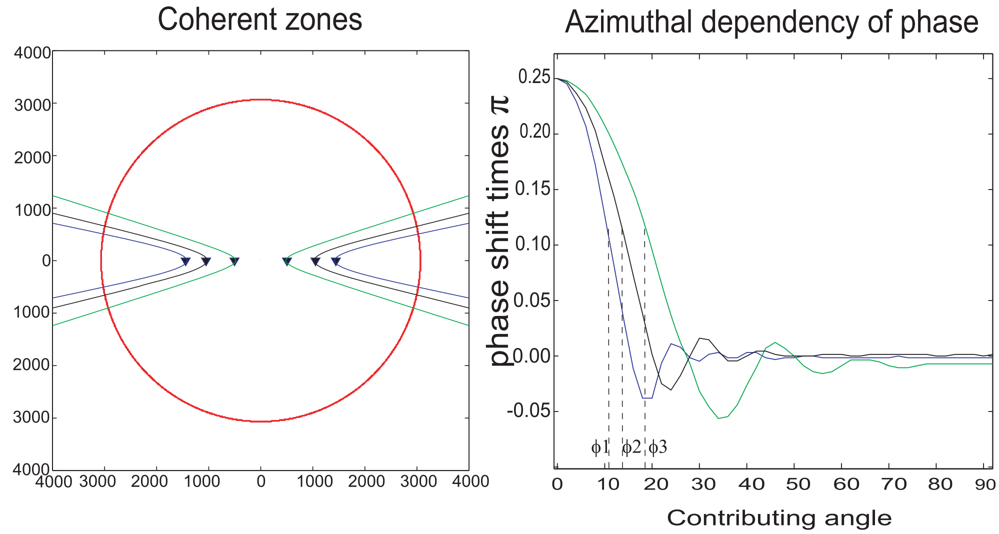

Figure 10. The left-hand side illustrates the coherent zones where sources interfere constructively. On the left we show the phase difference compared to the exact Green's function. When there are only sources on the source-receiver line ($\phi = 0$), the phase difference is $\pi/4$ as predicted by the theory.

Table 2. A different 1-D layered elastic medium with no attenuation.

	Thickness (m)	Vp ($\mathrm{m\,s^{-1}}$)	Vs ($\mathrm{m\,s^{-1}}$)	Density ($\mathrm{kg\,m^{-3}}$)
Layer 1	30	1700	360	700
Layer 2	470	1800	700	2000
Layer 3	770	2000	1260	2070
Layer 4	220	3100	1500	2300
Layer 5	830	4500	2760	2550
Layer 6	370	4400	2600	2525
Layer 7	220	3500	1850	2380
Layer 8	1.02×10^4	5500	3080	2600
Layer 9	9.4×10^3	6800	3900	2900
Layer 10	1.86×10^5	8000	4400	2600
Half-space	–	10 000	5200	3900

Note: It shows dispersion over a wider frequency range than Table 1.

thought important to consider again a certain ratio of wavelength to interstation distance. Bensen *et al.* (2007) advise as a lower limit to assume an interstation distance of at least 3λ, whereas the upper limit is constrained by attenuation and data limitations. The phase errors are plotted for seven different source coverages from the interstation line (Fig. 11, top left-hand side). The ratio of interstation distance over wavelength is plotted (top right-hand side), and the resulting angle of constructive interference (eq. 6, bottom left-hand side). The ratio of the source coverage over the angle of constructive interference is shown (bottom right-hand side). We see that in the frequency range of interest where $D/\lambda > 3$, phase errors can be persistent even if the coverage is larger than the angle of constructive interference. The significance of these errors are best expressed in terms of the resulting error in phase velocity, given by $\frac{\mathrm{d}c}{c} = \frac{\lambda}{2\pi D}\mathrm{d}\phi$. For example, an error of 1 per cent in $\mathrm{d}c/c$ occurs for a phase error $\mathrm{d}\phi = 0.06\pi$ for $D/\lambda = 3$. Fig. 12 shows this relative error for the phase velocity for different angles of azimuthal source coverage as a function of frequency. We see that with source coverages larger than 25° around the stationary phase point, the error remains smaller than 1 per cent. We confirm that the interstation distance smaller than 3λ would lead to large mistakes in phase velocity measurements, even if the coverage is wide.

5 CONVERGENCE TOWARDS THE EXACT GREEN'S FUNCTION

5.1 Convergence with uncorrelated and correlated sources

So far we have considered regularly distributed uncorrelated sources. To investigate retrieval with more realistic noise sources, we simulate a random wavefield. Sources are ignited randomly in strength, direction and location within a specified area at the free surface (Fig. 13). The model is the same as for Figs 2–9. We also consider sources overlapping in time which is more appropriate to simulate seismic noise (Bonnefoy-Claudet *et al.* 2006b; van Wijk 2006). At any given time, 20 sources (randomly from a location in Fig. 13) act simultaneously. Adding overlapping sources means that we cross correlate a longer and longer time-series, instead of summing cross correlations of responses from individual sources. Furthermore, we investigate the effect of the 1-bit approximation on convergence behaviour. The commonly applied 1-bit correlation is a time-normalization operation to use only the phase of the signal (Larose *et al.* 2004). Every positive value is set to 1 and every negative value to −1. Therefore we have the following four different input signals used as displacement in the applied cross correlation:

(i) the signal from uncorrelated sources,
(ii) their 1-bit equivalent,
(iii) the signal from correlated sources (overlapping in time) and
(iv) their 1-bit equivalent.

Examples of the four types of displacements in the correlations are shown in Fig. 14. Perhaps the 1-bit uncorrelated case is unrealistic for active experiments, polluted by noise. Zeroing out information below a certain amplitude threshold can overcome this. We progressively add more sources and monitor the converge to the exact Green's function.

Convergence is relatively fast in the case of uncorrelated sources; about 1000 sources for a correlation coefficient with respect to the true Green's function of 0.9. The final Green's function is much better than that of Figs 2 and 8. Having surface sources organized in a band helps to reduce the cross terms significantly (Draganov *et al.* 2004; Halliday & Curtis 2008). The 1-bit corresponding result

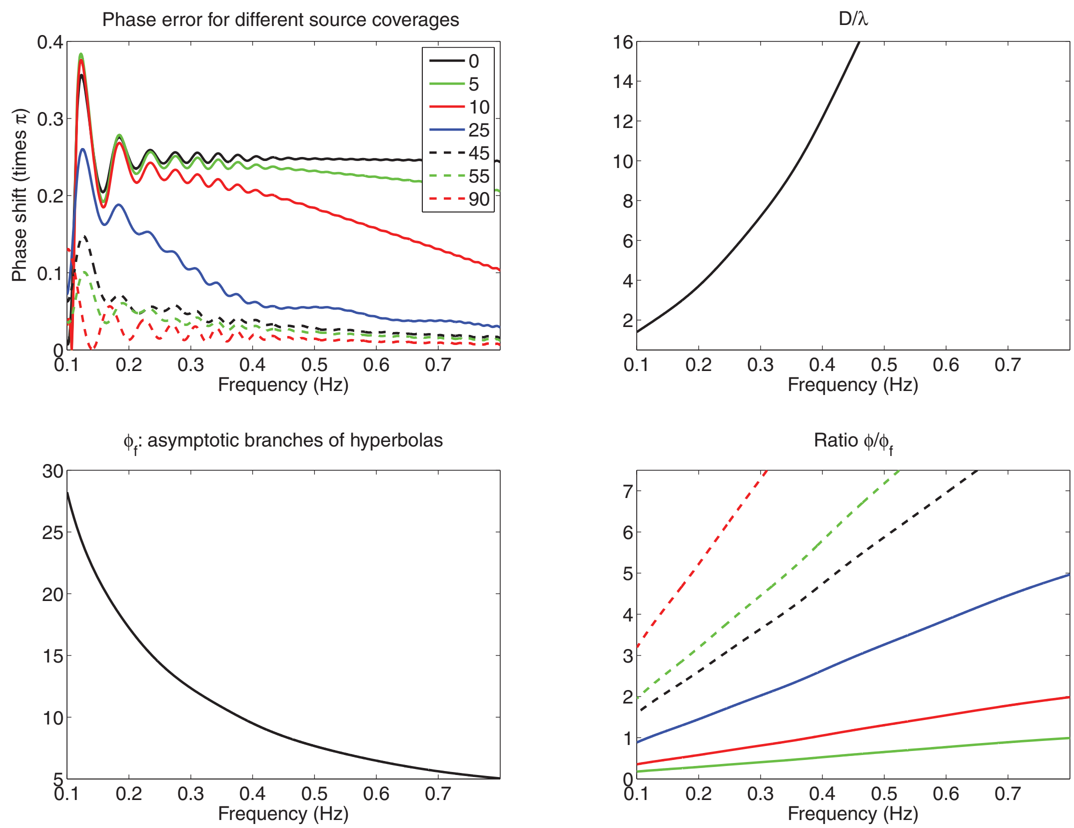

Figure 11. Top left-hand side shows the phase error resulting from different azimuthal source coverages around the interstation line. On the top right-hand side, the ratio of interstation distance over wavelength is plotted. (The limit of $D = 3\lambda$ occurs at 0.17 Hz). Bottom left-hand side shows the angular width of the coherent zone (eq. 5). The ratio of coverage angle over this angular width is plotted on the bottom right-hand side.

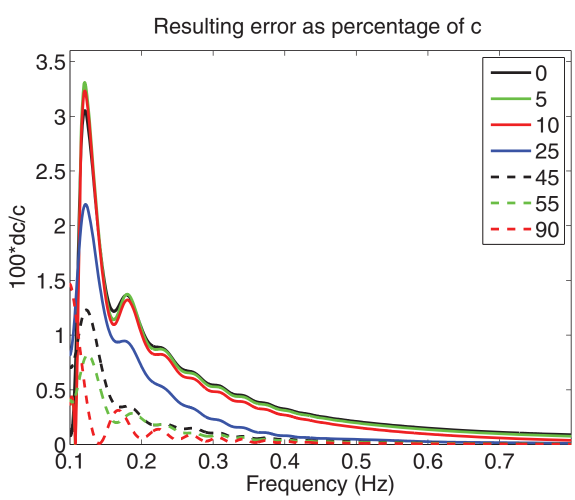

Figure 12. The resulting error in phase velocity ($\frac{dc}{c} = \frac{\lambda}{2\pi D} d\phi$) as a function of frequency.

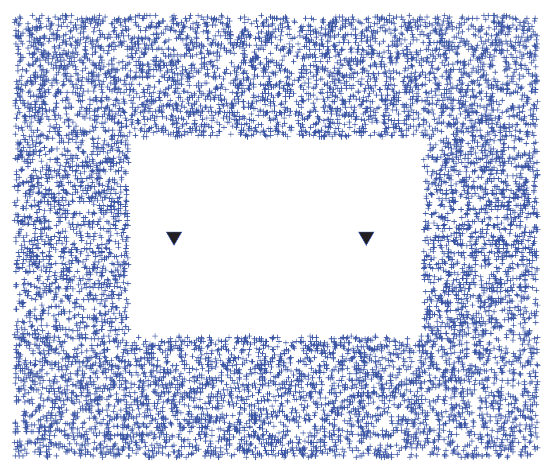

Figure 13. Configuration of source locations (blue), seen from above. All sources are at the free surface.

shows an overemphasized amplitude of the overtones. The phase, however, is correct.

In the case of overlapping sources, the sources are correlated in time only. The result is therefore expected to converge to the same result as the uncorrelated case (Wapenaar & Fokkema 2006), given enough averaging in time. Convergence is, as expected, much slower (about 10^6 sources for a correlation coefficient of 0.9).

The corresponding time required for convergence to the Green's function is quantified by Weaver & Lobkis (2005a,b). They define the factor of merit; the square of the signal-to-noise ratio. For surface waves this should be linear with the amount of sources or signal length that is used. We confirm this linear relationship over the analysed range for the fundamental mode.

5.2 Convergence of higher modes

There is a notable difference in the convergence behaviour of the higher modes compared to the fundamental mode. For correlated

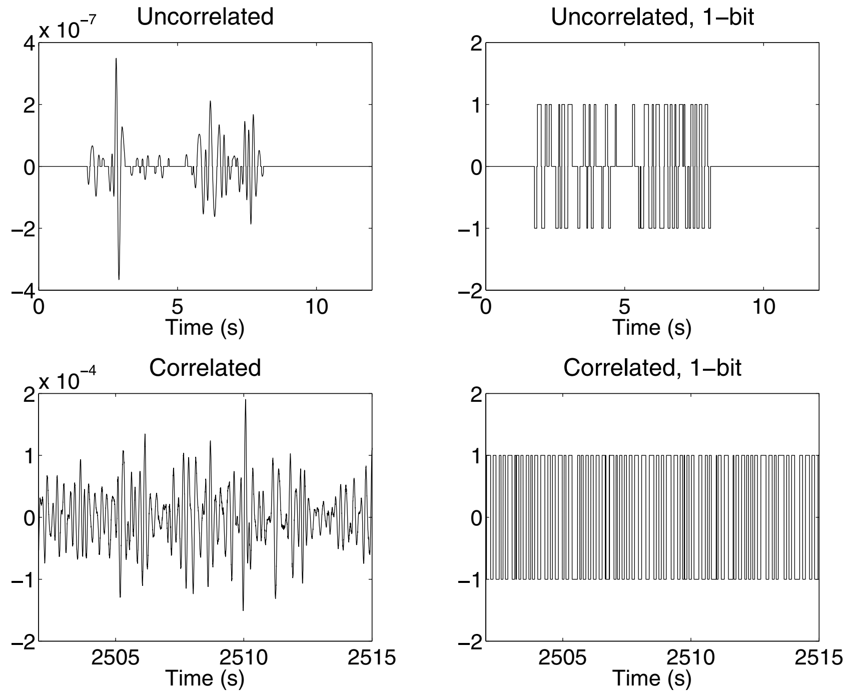

Figure 14. Typical time-series for the compared source and correlation types used. For uncorrelated sources, displacements from individual sources are correlated and summed (shown is the response in one receiver due to a single force in a random location and random direction, top left-hand side). The corresponding 1-bit seismogram makes no distinction in amplitude between higher modes and fundamental modes (top right-hand side). For correlated sources, on average 20 sources act simultaneously. Overlapping sources results in a longer signal in time, comparable to noise time-series. No coherent signal is distinguishable.

sources, the improvement of the match of higher modes sets in much slower than for the fundamental mode. This seems to be analogous to real data examples, where retrieval of higher modes is rare. To investigate this, we consider more specific criteria than the correlation coefficient; the total misfit of the envelope and instantaneous phase. We divide the seismograms in time windows corresponding to the fundamental mode and higher modes. We define the envelope and phase misfits as

$$M_A = \frac{\sum_{i=1}^{N} \left(A_i - A_i^{\text{direct}}\right)^2}{\sum_{i=1}^{N} \left(A_i^{\text{direct}}\right)^2}, \tag{7}$$

and

$$M_\phi = \frac{\sum_{i=1}^{N} \left[\cos(\phi_i) - \cos\left(\phi_i^{\text{direct}}\right)\right]^2}{\sum_{i=1}^{N} \left[\cos\left(\phi_i^{\text{direct}}\right)\right]^2}, \tag{8}$$

where A(t) and $\phi(t)$ are the envelope and instantaneous phase Bracewell (1965) of the signal, respectively. Together they constitute the analytical signal of the seismogram, which is constructed from the original signal and its Hilbert transform. The cosine is taken to prevent a bias by possible cycle-skips. The phase of the fundamental mode converges relatively fast for uncorrelated sources and somewhat slower for correlated sources (Fig. 15). This means, that a regime can exist, where the envelope is correctly retrieved, but still errors in phase exist. It is especially difficult to retrieve the correct phase of overtones using correlated sources (Fig. 15). However, in controlled source (uncorrelated) experiments, overtones can be retrieved using interferometric principles. This explains the observation of overtones in the active source experiments by Halliday *et al.* (2008) If we extrapolate on Fig. 15, to retrieve the correct phase of higher modes, we would need at least a time-series which is 100 times longer than that needed for the fundamental mode. In general, the envelope of the signal converges faster than the instantaneous phase, which means that it is more reliable to make group than phase velocity measurements.

5.3 Sources in coherent zones only

With correlated sources (such as ambient seismic noise), convergence is much slower than with uncorrelated sources (as in an active source experiment). However, observations of *P* waves from noise are reported in the literature (Roux *et al.* 2005b; Draganov *et al.* 2007, 2009). In the geometry of Roux *et al.* (2005b), the noise sources were only in the stationary phase regions by choosing the station pairs accordingly. To test if this would improve convergence, we only considered sources at the stationary phase regions given by eq. (6). Indeed we find that convergence is much faster for both the fundamental mode and the overtones (Fig. 16), the factor of merit increased roughly by a factor of 30. We observe again that we need about 100 times more sources, or 100 times longer time-series to achieve convergence for the higher modes. We speculate that using 100 times longer time-series would lead to convergence of higher modes for real data examples as well.

6 CONCLUSIONS

In this paper, we have considered a number of common approximations encountered in seismic interferometry and have studied their effects on the retrieved Green's functions. In particular, we have found that most of these approximations can seriously deteriorate the retrieval of the higher mode surface waves. Given that

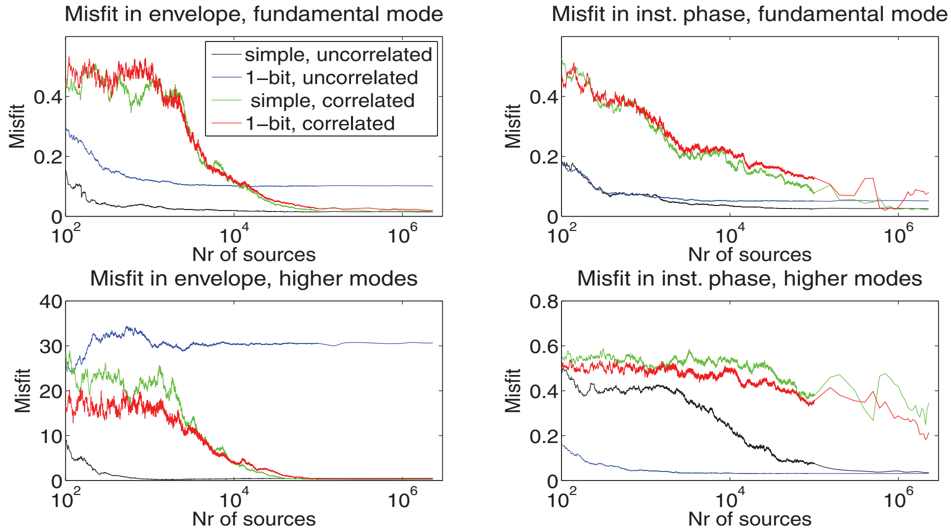

Figure 15. Misfit between the exact and retrieved envelope (left-hand side) and instantaneous phase (right-hand side) as a function of the amount of sources. For the case of correlated sources, adding more sources leads proportionally to a longer time-series. The values 10^4, 10^5 and 10^6 translate to a time-series of, respectively, 0.4, 4 and 40 hr. After 2.25×10^6 sources (90 hr), the phase of higher modes has still not completely converged.

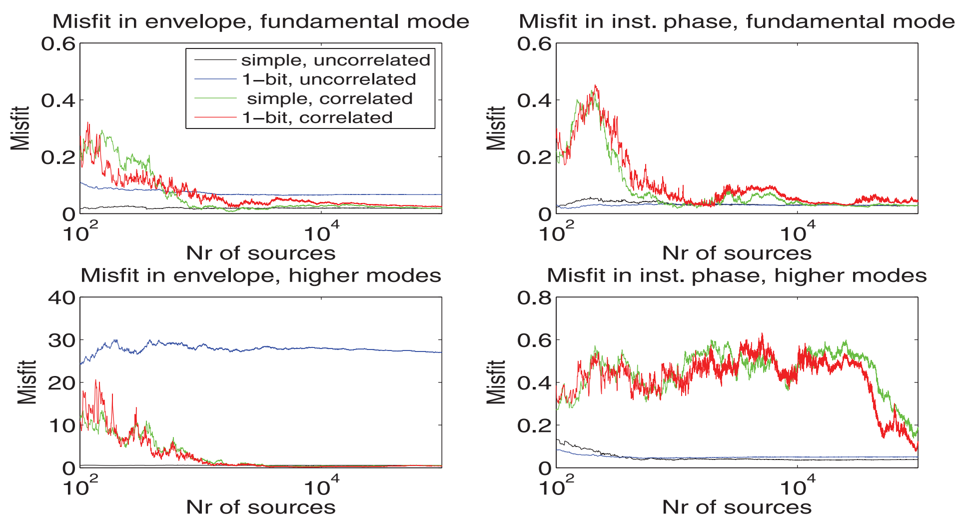

Figure 16. Misfits, for the case where sources are located in the coherent zones only. (Note the different scale, only up to 10^5 sources were used.)

the full wavefield is described by summation of individual surface wave modes, these conclusions apply to body wave studies as well. The main sources of error in the retrieved Green's function are (i) intermodal cross terms, (ii) incomplete cancellation of overlapping sources and (iii) incomplete coverage around the stationary phase region (dc/c in general smaller than 1 per cent for interstation distances larger than 3λ).

We found that with a complete integration surface, the point-force approximation applied to a full wavefield can still lead to intermodal cross terms. When sources are distributed at the surface only, cross terms can overwhelm the higher modes. However, the cross terms pose no problem if sources are distributed in bands (a thick boundary), or when sources are far away ($r/D > 12$).

Convergence towards the Green's function is considerably slower with correlated sources (overlapping in time). Two-order more sources or 100 times longer time-series are required before the higher modes start to converge. In our examples, phase and envelope have not yet converged unlike the solution of uncorrelated sources. Convergence is much faster when sources are at the stationary phase regions only, by a factor of 30. It thus appears that for retrieval of higher modes the directionality of noise can be used to our advantage. Roux *et al.* (2005b) describe the retrieval of body waves, where all interstation paths are taken in the prevalent noise direction. Most likely, these body waves would not have been observed under the same conditions if the noise field had been more omnidirectional.

ACKNOWLEDGMENTS

We are grateful for the comments by reviewers Sjoerd de Ridder, Jan Thorbecke and David Halliday that improved the manuscript. We thank Peter Moczo and Jozef Kristek for providing their codes and instructions. This work is part of the research programme of the Stichting voor Fundamenteel Onderzoek der Materie (FOM), which is financially supported by the Nederlandse Organisatie voor Wetenschappelijk Onderzoek (NWO). Computational resources for this work were provided by the Netherlands Research Center for

Integrated Solid Earth Science (ISES 3.2.5 High End Scientific Computation Resources).

REFERENCES

Aki, K. & Richards, P., 2002. *Quantitative Seismology*, 2nd edn, University science Books, Sausalito, USA.

Aldridge, D. & Symons, N., 2001. Seismic reciprocity rules, *SEG Expanded Abstracts,* **20,** 2049, doi:10.1190/1.1816548.

Bensen, G., Ritzwoller, M., Barmin, M., Levshin, A., Lin, F., Moschetti, M., Shapiro, N. & Yang, Y., 2007. Processing seismic ambient noise data to obtain reliable broad-band surface wave dispersion measurements, *Geophys. J. Int.,* **169,** 1239–1260, doi:10.1111/j.1365-246X.2007.03374.x.

Bonnefoy-Claudet, S., Cotton, F. & Bard, P.-Y., 2006a. The nature of noise wavefield and its applications for site effect studies: a literature review, *Earth-Sci. Rev.,* **79,** 205–227.

Bonnefoy-Claudet, S., Cornou, C., Bard, P.-Y., Cotton, F., Moczo, P., Kristek, J. & Fah, D., 2006b. H/v ratio: a tool for site effects evaluation. results from 1-d noise simulations, *Geophys. J. Int.,* **167**(2), 827–837.

Bracewell, R., 1965. The Fourier transform and its applications, in *The Fourier Transform and its Applications,* McGraw–Hill, New York, USA.

Campillo, M., 2006. Phase and correlation in 'random' seismic fields and the reconstruction of the green function, *Pure appl. Geophys.*, **163**, 475–502.

Campillo, M. & Paul, A., 2003. Long-range correlations in the diffuse seismic coda, *Science,* **299,** 547–549.

Curtis, A. & Robertsson, J.O.A., 2002. Volumetric wavefield recording and wave equation inversion for near-surface material properties, *Geophysics,* **67,** 1602–1611.

Curtis, A., Gerstoft, P., Sato, H., Snieder, R. & Wapenaar, K., 2006. Seismic interferometry: turning noise into signal, *Leading Edge,* **25**(9), 1082–1092.

de Hoop, A.D., 1995. *Handbook of Radiation and Scattering of Waves: Acoustic Waves in Fluids, Elastic Waves in Solids, Electromagnetic Waves,* Academic Press, London.

Derode, A., Larose, E., Tanter, M., de Rosny, J., Tourin, A., Campillo, M. & Fink, M., 2003. Recovering the Green's function from so-field correlations in an open scattering medium (l), *J. acoust. Soc. Am.,* **113**(6), 2973–2976.

Draganov, D., Wapenaar, K. & Thorbecke, J., 2004. Passive imaging in the presence of white noise sources, *Leading Edge,* **23**(9), 889–892.

Draganov, D., Wapenaar, K., Mulder, W., Singer, J. & Verdel, A., 2007. Retrieval of reflections from seismic background-noise measurements, *Geophys. Res. Lett.,* **34,** L04305.

Draganov, D., Campman, X., Thorbecke, J., Verdel, A. & Wapenaar, K., 2009. Reflection images from seismic noise, *Geophysics,* **74**(5), A63–A67.

Gerstoft, P., Shearer, P., Harmon, N. & Zhang, J., 2008. Global p, pp, and pkp wave microseisms observed from distant storms, *Geophys. Res. Lett.,* **35,** L23306, doi:10.1029/2008GL03111.

Gouédard, P. et al., 2008a. Cross-correlation of random fields: mathematical approach and applications, *Geophys. Prospect.,* **56**(3), 375–393.

Gouédard, P., Cornou, C. & Roux, P., 2008b. Phase-velocity dispersion curves and small-scale geophysics using noise correlation slantstack technique, *Geophys. J. Int.,* **172**(3), 971–981.

Halliday, D. & Curtis, A., 2008. Seismic interferometry, surface waves, and source distribution, *Geophys. J. Int.,* **175,** 1067–1087.

Halliday, D., Curtis, A. & Kragh, E., 2008. Seismic surface waves in a suburban environment: active and passive interferometric methods., *Leading Edge,,* **27**(2), 210–218.

Herrmann, R., 1978. Computer programs in earthquake seismology, volume 2: surface wave programs, *Tech. rep.,* Department of Earth and Atmospheric Sciences, Saint Louis University, NTIS PB, **292** 463.

Kristek, J., Moczo, P. & Archuleta, R., 2002. Efficient methods to simulate planar free surface in the 3d 4th-order staggered-grid finite-difference schemes, *Studia Geophysica et Geodaetica,* **46,** 355–381.

Larose, E., 2005. Diffusion multiple des ondes sismiques et experiences analogiques en ultrasons, *PhD thesis*, l'Universite Joseph Fourier, France.

Larose, E., Derode, A., Campillo, M. & Fink, M., 2004. Imaging from one-bit correlations of wideband diffuse wave fields, *J. appl. Phys.,* **95**(12), 8393–8399.

Lobkis, O. & Weaver, R., 2001. On the emergence of the Green's function in the correlations of a diffuse field, *J. acoust. Soc. Am.,* **110**(6), 3011–3017.

Longuet-Higgins, M., 1950. A theory of the origin of microseisms, *Phil. Trans. R. Soc. Lond., A,* **243,** 1–35.

Malcolm, A., Scales, J. & van Tiggelen, B., 2004. Extracting the green function from diffuse, equipartitioned waves, *Phys. Rev. E,* **70**(1), doi:10.1103/PhysRevE.70.015601.

Mehta, K., Snieder, R., Calvert, R. & Sheiman, J., 2008. Acquisition geometry requirements for generating virtual-source data, *The Leading Edge,* **27**(5), 620–629, doi:10.119011.2919580.

Moczo, P., Kristek, J., Vavrycuk, V., Archuleta, R. & Halada, L., 2002. 3d heterogeneous staggered-grid finite-difference modeling of seismic motion with volume harmonic and arithmetic averaging of elastic moduli and densities, *Bull. seism. Soc. Am.,* **92**(8), 3042–3066.

Nishida, K., Montagner, J.-P. & Kawakatsu, H., 2009. Global surface wave tomography using seismic hum, *Science,* **326**(5949), 112, doi:10.1126/science.1176389.

Nolet, G., Sleeman, R., Nijhof, V. & Kennett, B.L.N., 1989. Synthetic reflection seismograms in three dimensions by a locked-mode approximation, *Geophysics,* **54**(3), 350–358.

Picozzi, M., Parolai, S., Bindi, D. & Strollo, A., 2009. Characterization of shallow geology by high-frequency seismic noise tomography, *Geophys. J. Int.,* **176**(1), 164–174.

Rhie, J. & Romanowicz, B., 2004. Excitation of earth's continuous free oscillations by atmosphere-ocean-seafloor coupling, *Nature,* **431,** 552–556.

Roux, P., 2009. Passive seismic imaging with directive ambient noise: application to surface waves and the San Andreas Fault in parkfield, CA, *Geophys. J. Int.,* **179,** 367–373.

Roux, P., Sabra, K. & Kuperman, W., 2005a. Ambient noise cross correlation in free space: theoretical approach, *J. acoust. Soc. Am.,* **117**(1), 79–84.

Roux, P., Sabra, K.G., Gerstoft, P., Kuperman, W.A. & Fehler, M.C., 2005b. P-waves from cross-correlation of seismic noise, *Geophys. Res. Lett.,* **32,** L19303.

Sabra, K., Gerstoft, P., Roux, P., Kuperman, W. & Fehler, M., 2005. Surface wave tomography from microseisms in southern California, *Geophys. Res. Lett.,* **32, L**14311.

Sanchez-Sesma, F. & Campillo, M., 2006. Retrieval of the Green's function from cross correlation: the canonical elastic problem, *Bull. seism. Soc. Am.,* **96**(3), 1182–1191.

Shapiro, N., Campillo, M., Stehly, L. & Ritzwoller, M., 2005. High resolution surface wave tomography from ambient seismic noise, *Science,* **307,** 1615–1618.

Snieder, R., 2002. Scattering of surface waves, in *Scattering of surface waves, in Scattering and Inverse Scattering in Pure and Applied Science,* pp. 562–577, Academic Press, San Diego.

Snieder, R., 2004. Extracting the Green's function from the correlation of coda waves: a derivation based on stationary phase, *Phys. Rev. E.,* **69,** 046610, doi:10.1103.PhysRevE.69.046610.

Snieder, R., Wapenaar, K. & Larner, K., 2006. Spurious multiples in seismic interferometry of primaries, *Geophysics,* **71**(4), SI111–SI124.

Snieder, R., Miyazawa, M., Slob, E. & Vasconcelos, I., 2009. A comparison of strategies for seismic interferometry, *Surv. Geophys.,* **30**(4-5), 503–523.

Stehly, L., Campillo, M. & Shapiro, N., 2006. A study of the seismic noise from its long-range correlation properties, *J. geophys. Res.,* **111**(B10), B10306 [0148–0227].

Tanimoto, T., Ishimaru, S. & Alvizuri, C., 2006. Seasonality in particle motion of microseisms, *Geophys. J. Int.,* **166,** 253–266.

Tsai, V., 2009. On establishing the accuracy of noise tomography travel-time measurements in a realistic medium, *Geophys. J. Int.,* **178,** 1555–1564, doi:10.1111/j.1365-246X.2009.04239.x.

van Manen, D.J., Curtis, A. & Robertsson, J.O.A., 2006. Interferometric modelling of wave propagation in inhomogeneous elastic media using time-reversal and reciprocity, *Geophysics,* **71**(4), SI47–SI60.

van Wijk, K., 2006. On estimating the impulse response between receivers in a controlled ultrasonic experiment, *Geophysics,* **71**(4), SI79–SI84.

Wapenaar, K., 2004. Retrieving the elastodynamic Green's function of an arbitrary inhomogeneous medium by cross correlation, *Phys. Rev. Lett.,* **93,** 254301.
Wapenaar, K. & Fokkema, J., 2006. Green's function representations for seismic interferometry, *Geophysics,* **71**(4), SI33–SI46.
Wapenaar, K., Slob, E. & Snieder, R., 2008. Seismic and electromagnetic controlled-source interferometry in dissipative media, *Geophys. Prospect.,* **56,** 419–434.
Weaver, R. & Lobkis, O., 2001. Ultrasonics without a source: thermal fluctuation correlations at MHz frequencies, *Phys. Rev. Lett.,* **87**(13), 134301.
Weaver, R.L. & Lobkis, O.I., 2005a. Fluctuations in diffuse field–field correlations and the emergence of the Green's function in open systems, *J. acous. Soc. Am.,* **117**(6), 3432–3439.
Weaver, R.L. & Lobkis, O.I., 2005b. The mean and variance of diffuse field correlations in finite bodies, *J. acoust. Soc. Am.,* **118**(6), 3447–3456.
Yang, Y., Ritzwoller, M., Levshin, A.L. & Shapiro, N.M., 2007. Ambient noise Rayleigh wave tomography across Europe, *Geophys. J. Int.,* **168**(1), 259–274.
Yao, H. & van der Hilst, R., 2009. Analysis of ambient noise energy distribution and phase velocity bias in ambient noise tomography, with application to se tibet, *Geophys. J. Int.,* **179**(2), 1113–1132.
Yao, H., Campman, X., de Hoop, M.V. & van der Hilst, R.D., 2009. Estimation of surface wave Green's functions from correlation of direct waves, coda waves, and ambient noise in se tibet, *Phys. Earth planet. Inter.,* **77**(1-2), 1 – 11.

APPENDIX A: SINGLE-MODE RAYLEIGH WAVE INTERFEROMETRY

For a homogeneous isotropic medium the elasticity tensor only depends on the Lamé parameters λ and μ.

$$c_{pjkq} = \lambda\delta_{pj}\delta_{kq} + \mu(\delta_{pk}\delta_{jq} + \delta_{pq}\delta_{jk}). \tag{A1}$$

We subsitute indices p and q in eq. (1) for n and l, respectively. In a layered medium, λ and μ are functions of depth (Aki & Richards 2002). Eq. (1) is valid for the full wave Green's function ($\sum_n G^n$), but also for isolated modes (G^n). We will now consider an isolated mode, and drop n. Eq. (1) becomes

$$\begin{aligned} G_{im}(\mathbf{x_A}, \mathbf{x_B}, \omega) - G^*_{im}(\mathbf{x_A}, \mathbf{x_B}, \omega) = \oint_S &[\lambda\delta_{pj}\delta_{kq} + \mu(\delta_{pk}\delta_{jq} + \delta_{pq}\delta_{jk})]n_j[\partial_k G^*_{mq}(\mathbf{x_B}, \mathbf{x}, \omega)G_{ip}(\mathbf{x_A}, \mathbf{x}, \omega) \\ &- \partial_k G_{iq}(\mathbf{x_A}, \mathbf{x}, \omega)G^*_{mp}(\mathbf{x_B}, \mathbf{x}, \omega)]\mathrm{d}S. \end{aligned} \tag{A2}$$

The material parameters are at the source location on the integration surface. We assume a cylindrical surface with radius r (Fig. A1). The angle of the normal with the x-axis is defined as ϕ. Eq. (7.147) in Aki & Richards gives the far field Rayleigh wave Green's tensor due to a point force excitation in a layered (laterally invariant) medium. The partial derivative in the k-direction gives

$$\partial_k G_{iq}(\mathbf{x_A}) = \begin{pmatrix} -ik\cos(\phi_1)G_{ix}(\mathbf{x_A}) & -ik\cos(\phi_1)G_{iy}(\mathbf{x_A}) & -ik\cos(\phi_1)G_{iz}(\mathbf{x_A}) \\ -ik\sin(\phi_1)G_{ix}(\mathbf{x_A}) & -ik\sin(\phi_1)G_{iy}(\mathbf{x_A}) & -ik\sin(\phi_1)G_{iz}(\mathbf{x_A}) \\ \frac{\partial r_1}{\partial z}|_h \frac{1}{r_1(h)}G_{ix}(\mathbf{x_A}) & \frac{\partial r_1}{\partial z}|_h \frac{1}{r_1(h)}G_{iy}(\mathbf{x_A}) & \frac{\partial r_2}{\partial z}|_h \frac{1}{r_2(h)}G_{iz}(\mathbf{x_A}) \end{pmatrix}. \tag{A3}$$

r_1 and r_2 are the Rayleigh wave eigenfunctions of the mode under consideration, h is the source depth. (The angle towards receiver $\mathbf{x_A}$ is ϕ_1, and towards receiver $\mathbf{x_B}$ is ϕ_2.)

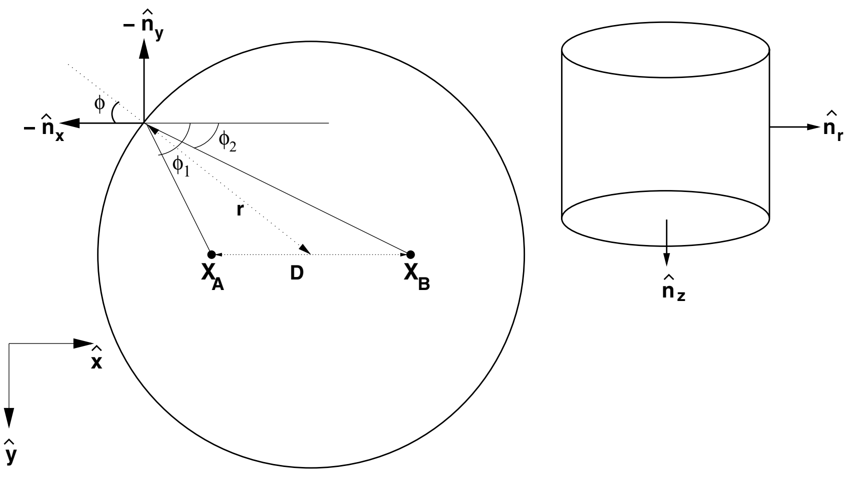

Figure A1. View from above (left-hand side) and view from the side (right-hand side). The normals are zero in the z direction, except at the bottom layer.

Substituting eq. (A3) and its complex conjugate into eq. (A2) leads to the interferometry equation in terms of surface waves

$$
\begin{aligned}
G_{im}(\mathbf{x_A}, \mathbf{x_B}, \omega) - G^*_{im}(\mathbf{x_A}, \mathbf{x_B}, \omega) = \oint_S & n_x(\lambda+\mu)ik(\cos(\phi_1)+\cos(\phi_2))G_{ix}(\mathbf{x_A})G^*_{mx}(\mathbf{x_B}) \\
&+ n_y(\lambda+\mu)ik(\sin(\phi_1)+\sin(\phi_2))G_{iy}(\mathbf{x_A})G^*_{my}(\mathbf{x_B}) \\
&+ n_x ik(\lambda\sin(\phi_1)+\mu\sin(\phi_2))[G_{ix}(\mathbf{x_A})G^*_{my}(\mathbf{x_B})+G_{iy}(\mathbf{x_A})G^*_{mx}(\mathbf{x_B})] \\
&+ n_y ik(\lambda\cos(\phi_1)+\mu\cos(\phi_2))[G_{iy}(\mathbf{x_A})G^*_{mx}(\mathbf{x_B})+G_{ix}(\mathbf{x_A})G^*_{my}(\mathbf{x_B})] \\
&- n_x\left[\lambda \left.\frac{\partial r_2}{\partial z}\right|_h \frac{1}{r_2(h)}\left(G_{ix}(\mathbf{x_A})G^*_{mz}(\mathbf{x_B})-G_{iz}(\mathbf{x_A})G^*_{mx}(\mathbf{x_B})\right)\right. \\
&\left.+ \mu \left.\frac{\partial r_1}{\partial z}\right|_h \frac{1}{r_1(h)}(G_{iz}(\mathbf{x_A})G^*_{mx}(\mathbf{x_B})-G_{ix}(\mathbf{x_A})G^*_{mz}(\mathbf{x_B}))\right] \\
&- n_y\left[\lambda \left.\frac{\partial r_2}{\partial z}\right|_h \frac{1}{r_2(h)}(G_{iy}(\mathbf{x_A})G^*_{mz}(\mathbf{x_B})-G_{iz}(\mathbf{x_A})G^*_{my}(\mathbf{x_B}))\right. \\
&\left.+ \mu \left.\frac{\partial r_1}{\partial z}\right|_h \frac{1}{r_1(h)}(G_{iz}(\mathbf{x_A})G^*_{my}(\mathbf{x_B})-G_{iy}(\mathbf{x_A})G^*_{mz}(\mathbf{x_B}))\right] \\
&+ ik\mu\left[n_x((\cos(\phi_1)+\cos(\phi_2))(G_{ix}(\mathbf{x_A})G^*_{mx}(\mathbf{x_B})+G_{iy}(\mathbf{x_A})G^*_{my}(\mathbf{x_B})+G_{iz}(\mathbf{x_A})G^*_{mz}(\mathbf{x_B})))\right. \\
&\left.+ n_y((\sin(\phi_1)+\sin(\phi_2))(G_{ix}(\mathbf{x_A})G^*_{mx}(\mathbf{x_B})+G_{iy}(\mathbf{x_A})G^*_{my}(\mathbf{x_B}))+G_{iz}(\mathbf{x_A})G^*_{mz}(\mathbf{x_B})\right]\mathrm{d}S
\end{aligned}
\tag{A4}
$$

Here we left out the n_z terms for the sake of brevity, as their total contribution will sum to zero. Also, from the top and the bottom of the cylinder, the contribution is zero due to the boundary conditions (free surface and radiation condition). On the side, the normals are defined as

$$
n_x = -\cos(\phi_0), \quad n_y = -\sin(\phi_0), \quad n_z = 0. \tag{A5}
$$

We assume sources far away from A and B, that is, $\phi_1 \approx \phi_2 \approx \phi_0 \approx \phi$. Furthermore, the following relations exist between the different components in the Green's tensor (Aki & Richards 2002):

$$
\begin{aligned}
&\sin(\phi)G_{ix}(\mathbf{x_A}) = \cos(\phi)G_{iy}(\mathbf{x_A}) \\
&r_2(h)G_{ix}(\mathbf{x_A}) = i\cos(\phi)G_{iz}(\mathbf{x_A})r_1(h) \\
&r_2(h)G_{iy}(\mathbf{x_A}) = i\sin(\phi)G_{iz}(\mathbf{x_A})r_1(h)
\end{aligned}
\tag{A6}
$$

Eq. (A4) then simplifies to

$$
\begin{aligned}
G_{im}(\mathbf{x_A}, \mathbf{x_B}, \omega) - G^*_{im}(\mathbf{x_A}, \mathbf{x_B}, \omega) \approx -2ik\int_0^{2\pi}\int_0^{\infty} & \left(\left(\lambda+2\mu+\lambda \left.\frac{\partial r_2}{\partial z}\right|_h \frac{1}{kr_1(h)}\right)(G_{ix}(\mathbf{x_A})G^*_{mx}(\mathbf{x_B})+G_{iy}(\mathbf{x_A})G^*_{my}(\mathbf{x_B}))\right. \\
&\left.+\left(\mu-\mu \left.\frac{\partial r_1}{\partial z}\right|_h \frac{1}{kr_2(h)}\right)G_{iz}(\mathbf{x_A})G^*_{mz}(\mathbf{x_B})\right) r\,\mathrm{d}\phi\mathrm{d}z.
\end{aligned}
\tag{A7}
$$

By using the fundamental (but only meaningful for isolated modes) relation between surface wave energy integrals (Halliday & Curtis 2008) $I_2 + I_3/2k = cUI_1$, this can be simplified to

$$
G_{im}(\mathbf{x_A}, \mathbf{x_B}, \omega) - G^*_{im}(\mathbf{x_A}, \mathbf{x_B}, \omega) \approx -2i\omega U(\omega)\int_0^{\infty}\int_0^{2\pi} \rho G_{ip}(\mathbf{x_A})G^*_{mp}(\mathbf{x_B}) r\,\mathrm{d}\phi\mathrm{d}z. \tag{A8}
$$

APPENDIX B: SINGLE-MODE LOVE WAVE INTERFEROMETRY

Following the same procedure for Love waves, the partial derivative of the Green's tensor is given by

$$
\partial_k G_{iq} = \begin{pmatrix} -ik\cos(\phi)G_{ix} & -ik\cos(\phi)G_{iy} & 0 \\ -ik\sin(\phi)G_{ix} & -ik\sin(\phi)G_{iy} & 0 \\ \left.\frac{\partial l_1}{\partial z}\right|_h \frac{1}{l_1(h)}G_{ix} & \left.\frac{\partial l_1}{\partial z}\right|_h \frac{1}{l_1(h)}G_{iy} & 0 \end{pmatrix}, \tag{B1}
$$

with l_1 the Love wave displacement eigenfunction. Substituting this (and its complex conjugate) into eq. (A2) and simplification leads to

$$G_{im}(\mathbf{x_A}, \mathbf{x_B}, \omega) - G^*_{im}(\mathbf{x_A}, \mathbf{x_B}, \omega) \approx -2ik \int_0^\infty \int_0^{2\pi} 2\mu(z)(G_{ix}(\mathbf{x_A})G^*_{mx}(\mathbf{x_B}) + G_{iy}(\mathbf{x_A})G^*_{my}(\mathbf{x_B}))r\,\mathrm{d}\phi\,\mathrm{d}z. \quad \text{(B2)}$$

For Love waves the z-derivative terms cancel. By using the identity $I_2 = cI_1U$ (Aki & Richards 2002) in eq. (B2) we find again

$$G_{im}(\mathbf{x_A}, \mathbf{x_B}, \omega) - G^*_{im}(\mathbf{x_A}, \mathbf{x_B}, \omega) \approx -2i\omega U(\omega) \int_0^\infty \int_0^{2\pi} \rho G_{ip}(\mathbf{x_A})G^*_{mp}(\mathbf{x_B})r\,\mathrm{d}\phi\,\mathrm{d}z, \quad \text{(B3)}$$

but now with $U(\omega)$ as the Love wave group velocity.